Modeling Acquisition Geometries with Improved Super-Resolution in Digital Breast Tomosynthesis

Raymond J. Acciavatti[a], E. Paul Wileyto[b], and Andrew D. A. Maidment[a]

Departments of [a]Radiology, [b]Biostatistics and Epidemiology

Perelman School of Medicine at the University of Pennsylvania, Philadelphia PA 19104

E-mail: {Raymond.Acciavatti@uphs | epw@mail.med | Andrew.Maidment@uphs}.upenn.edu

ABSTRACT

In digital breast tomosynthesis (DBT), a reconstruction is created from multiple x-ray projection images. Our previous work demonstrated that the reconstruction is capable of super-resolution (*i.e.*, subpixel resolution) relative to the detector. In order for super-resolution to yield a reliable improvement in image quality, it should be achievable at all positions in the reconstruction. This paper demonstrates that super-resolution is not achievable at all depths, or at all heights above the breast support. For this purpose, a bar pattern phantom was imaged using a commercial DBT system. A goniometry stand was used to orient the long axis of the parallel bars along an oblique plane relative to the breast support. This setup allowed a single test frequency to be visualized over a continuous range of depths. The orientation of the test frequency was parallel to the direction of x-ray tube motion. An oblique reconstruction in the plane of the bar pattern phantom showed that the existence of super-resolution is depth-dependent. To identify design strategies for optimizing super-resolution, a theoretical model was then developed in which a test frequency higher than the alias frequency of the detector was simulated. Two design modifications that improve super-resolution are identified. In particular, it is shown that reducing the spacing between the x-ray source positions minimizes the number of depths lacking super-resolution. Additionally, introducing detector motion along the direction perpendicular to the breast support allows for more uniform super-resolution throughout the image volume. In conclusion, this work presents strategies for optimizing super-resolution in DBT.

Keywords: Digital breast tomosynthesis (DBT), super-resolution, aliasing, bar pattern phantom, image reconstruction, mathematical modeling, Fourier transform, calcifications.

1. INTRODUCTION

Digital breast tomosynthesis (DBT) is now being offered by many medical centers for breast cancer screening. The 3D DBT image is interpreted in combination with either a 2D digital mammography (DM) image or a synthetic 2D image, depending on the center. Various studies have demonstrated the benefits of 3D/2D imaging over conventional 2D imaging.[1-3] One such work by Rafferty *et al*. used receiver operating characteristic (ROC) methods in a reader study.[2] Rafferty *et al*. showed that DBT/DM is characterized by a higher area under the ROC curve than DM alone. To determine whether the benefits of DBT/DM were limited to a specific subgroup of lesions, Rafferty *et al*. also performed the ROC analysis separately for masses and calcifications. It was determined that the higher area under the ROC curve was seen only in the imaging of masses. There was effectively no change in reader performance in the imaging of calcifications.

Our previous work demonstrated that super-resolution is a technique for improving the visibility of calcifications in DBT. Super-resolution is a term which describes the visualization of higher frequencies than the alias frequency of the detector. A necessary condition for super-resolution is that the pixelation of the reconstruction must be smaller than the detector element size. With an anecdotal example, we showed that super-resolution yields a sharper image of calcifications with finer detail.[4]

Super-resolution needs to be achieved at all positions in the image volume in order for calcification visibility to be improved reliably. Our previous work showed that DBT systems are not yet designed to maximize the positions at which super-resolution is achievable. This result was demonstrated with theoretical modeling using a sinusoidal test object. First, the frequency of the object was oriented along the direction perpendicular to the plane of x-ray tube

motion; *i.e.*, along the posteroanterior (PA) direction. Super-resolution was not achieved at most positions in the image volume. Second, the frequency was oriented along the direction of x-ray tube motion; this direction is left-to-right in a cranial-caudal (CC) view and is superior-to-inferior in a mediolateral (ML) view. Super-resolution was achieved at considerably more positions, but there were anisotropies at some heights (*z*) above the breast support.[4]

Medical imaging systems commonly evolve over multiple generations. Many of the principles that guided the evolution of computed tomography (CT) scanners can be applied to the design of DBT systems. The positioning of the detector elements in a third-generation CT scanner provides a useful illustration of this concept. The CT scanner is designed so that the centroid of the detector element is shifted relative to the iso-center by one-quarter of the detector element size. For example, in a detector with 1.0 mm pixelation, the shift is 0.25 mm. It has been shown that this design strategy maximizes the range of frequencies that can be successfully imaged without aliasing.[5]

With theoretical modeling, a similar design was proposed for DBT in our previous work. In this new design, the detector is translated along the PA direction during the scan time, with the increment of translation per projection being a fraction of detector element length. It was shown that this design allows super-resolution to be achieved over a broad range of positions along the PA direction, unlike a conventional DBT system.[6] This design strategy is similar to the one seen in a third-generation CT scanner, in that a subpixel shift in detector element positioning is used to increase the range of frequencies that can be visualized.

Although a design was proposed for optimizing super-resolution along the PA direction, there has been no analogous study for optimizing super-resolution along the direction of x-ray tube motion. In this paper, a sinusoidal test object will be used to identify designs that maximize the number of positions exhibiting super-resolution along this direction. Initially, the conventional design for DBT will be modeled. We will determine whether super-resolution can be optimized simply by changing the values for the acquisition parameters of this design. These parameters include the angular range of the x-ray tube motion and the number of projections. Subsequently, we will determine whether a new form of detector motion yields benefits not achievable with the conventional design. The new detector motion is oriented along the *z* direction perpendicular to the breast support; it is an alternative to the PA detector motion that was proposed in our previous paper.

2. METHODS

### 2.1 Test Object and Design Parameters
A sinusoidal input is now modeled as a test object for DBT. This object can be used to investigate super-resolution assuming that the input frequency is larger than the alias frequency of the detector. Figure 1 shows a cross section of this object in the plane of x-ray tube motion (*i.e.*, the plane of the chest wall). This plane is defined as the *xz* plane. The cross section of the object is rectangular with thickness ε and frequency f_0. Also, the mid-thickness of the object is positioned at the height $z = z_0$. The equation for this object is

$$\mu = C_{\text{obj}} \cdot \cos\left(2\pi f_0 \left[(x - x_0)\cos\alpha + (y - y_0)\sin\alpha\right]\right) \cdot \text{rect}\left(\frac{z - z_0}{\varepsilon}\right), \quad \text{rect}(u) \equiv \begin{cases} 1, & |u| \le 1/2 \\ 0, & |u| > 1/2 \end{cases}, \tag{1}$$

where μ is the attenuation coefficient of the object, C_{obj} is the amplitude of the waveform, and x_0 and y_0 are coordinates that control the position of the peak. As shown, the input frequency is oriented along the polar angle α in a plane parallel to the breast support (Figure 2). In addition, the (x, y, z) coordinate of each point in space is measured relative to point O (the origin). Unlike previous work[4] in which the origin was defined as a point on the detector, the origin is now defined as a point on the breast support. Specifically, the origin is the midpoint of the chest wall side of the breast support. The origin is chosen in this manner so that point O is stationary during the scan time regardless of the new forms of detector motion that are considered.

It is now useful to determine the coordinate of the focal spot at point A. In the central projection, the focal spot has the coordinate $(0, 0, z_{\text{DM}})$ relative to the origin O. This notation emphasizes that this coordinate is equivalent to the focal spot position in a conventional 2D digital mammography (DM) image. As the focal spot sweeps the angle ψ, the position of point A can be described by the more general coordinate $(x_{\text{FS}}, 0, z_{\text{FS}})$

$$\overrightarrow{OA} = x_{\text{FS}}\mathbf{i} + z_{\text{FS}}\mathbf{k}, \quad x_{\text{FS}} = (z_{\text{DM}} - z_{\text{COR}})\sin\psi, \quad z_{\text{FS}} = z_{\text{COR}} + (z_{\text{DM}} - z_{\text{COR}})\cos\psi, \tag{2}$$
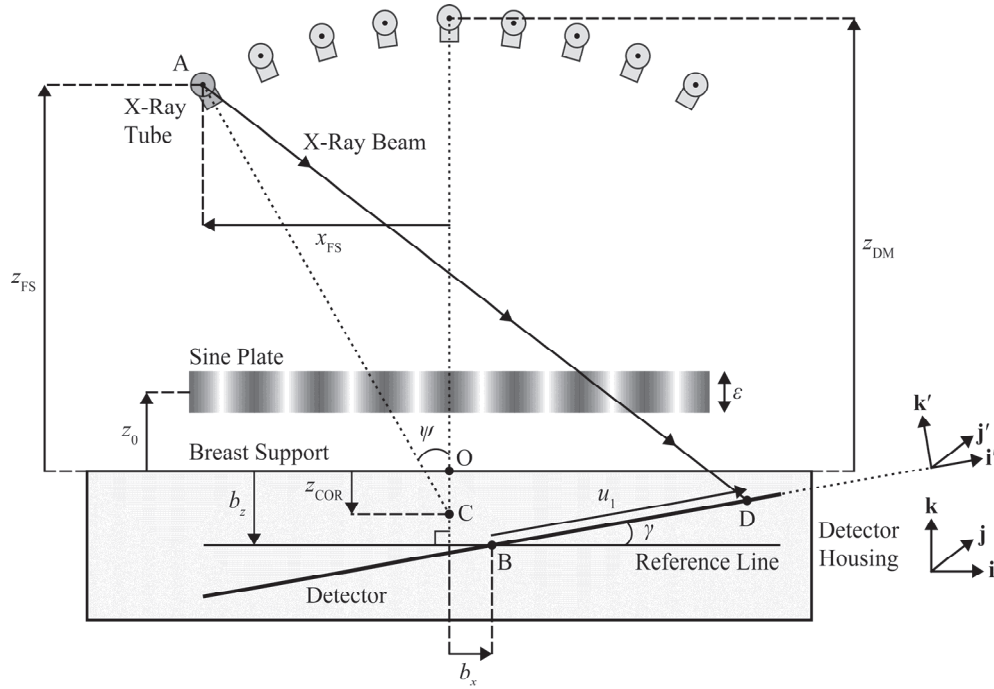
Figure 1. In DBT, the x-ray source rotates in a circular arc within the xz plane. Although detector rotation is found in some clinical DBT systems, an additional form of detector motion that is considered is an arbitrary translation of point B.

where z_{COR} is the z-coordinate of the center-of-rotation (COR) of x-ray tube motion (point C). The projection angle ψ can in turn be determined from the projection number (n) and the angular spacing between projections ($\Delta\psi$): $\psi = [n - 1 - (N - 1)/2] \cdot \Delta\psi$. In this expression, the projection number (n) varies in integer steps from 1 to N.

2.2 Calculation of the Projection Images

The detected signal is now calculated as a function of position relative to the origin O. This paper models detector translation during the scan time by considering the motion of a fixed reference point (B) on the detector. Specifically, point B is the midpoint of the chest wall side of the detector. The translational shift of point B relative to the origin can be expressed using the position vector: $\overrightarrow{OB} = b_x\mathbf{i} + b_y\mathbf{j} + b_z\mathbf{k}$. In Section 3.3, the shift parameters b_x, b_y, and b_z are written as a function of time for different forms of detector motion that are proposed. In addition to detector translation, detector rotation is modeled in this paper. Detector rotation is found in some clinical systems such as the Selenia Dimensions system (Hologic Inc., Bedford, MA), in which the detector is rotated by the angle γ about the y axis. By rotating the basis vectors by this angle, it can be shown that the basis vectors for the primed coordinate system are

$$\begin{pmatrix} \mathbf{i}' \\ \mathbf{j}' \\ \mathbf{k}' \end{pmatrix} = \begin{pmatrix} \cos\gamma & 0 & \sin\gamma \\ 0 & 1 & 0 \\ -\sin\gamma & 0 & \cos\gamma \end{pmatrix} \begin{pmatrix} \mathbf{i} \\ \mathbf{j} \\ \mathbf{k} \end{pmatrix}, \qquad \gamma = \frac{-\psi}{g}. \tag{3}$$

In this expression, the detector rotation angle (γ) is written in terms of the projection angle (ψ) and the gear ratio (g). Assuming that an arbitrary detector position (D) has the coordinate (u_1, u_2) measured in the plane of the detector relative to point B (Figure 2), the position vector for this point can be calculated by using the primed basis vectors.

$$\overrightarrow{BD} = u_1\mathbf{i}' + u_2\mathbf{j}' = (u_1\cos\gamma)\mathbf{i} + u_2\mathbf{j} + (u_1\sin\gamma)\mathbf{k} \tag{4}$$

To determine the detected signal at point D, a line integral is now calculated by tracing a ray from point A to point D. This ray can be described by the position vector: $\overrightarrow{AD} = \overrightarrow{AO} + \overrightarrow{OB} + \overrightarrow{BD} = -\overrightarrow{OA} + \overrightarrow{OB} + \overrightarrow{BD} = \zeta_x\mathbf{i} + \zeta_y\mathbf{j} + \zeta_z\mathbf{k}$. In this expression, ζ_x, ζ_y, and ζ_z are defined as follows.

$$\zeta_x = u_1\cos\gamma + b_x - x_{FS}, \qquad \zeta_y = u_2 + b_y, \qquad \zeta_z = u_1\sin\gamma + b_z - z_{FS} \tag{5}$$
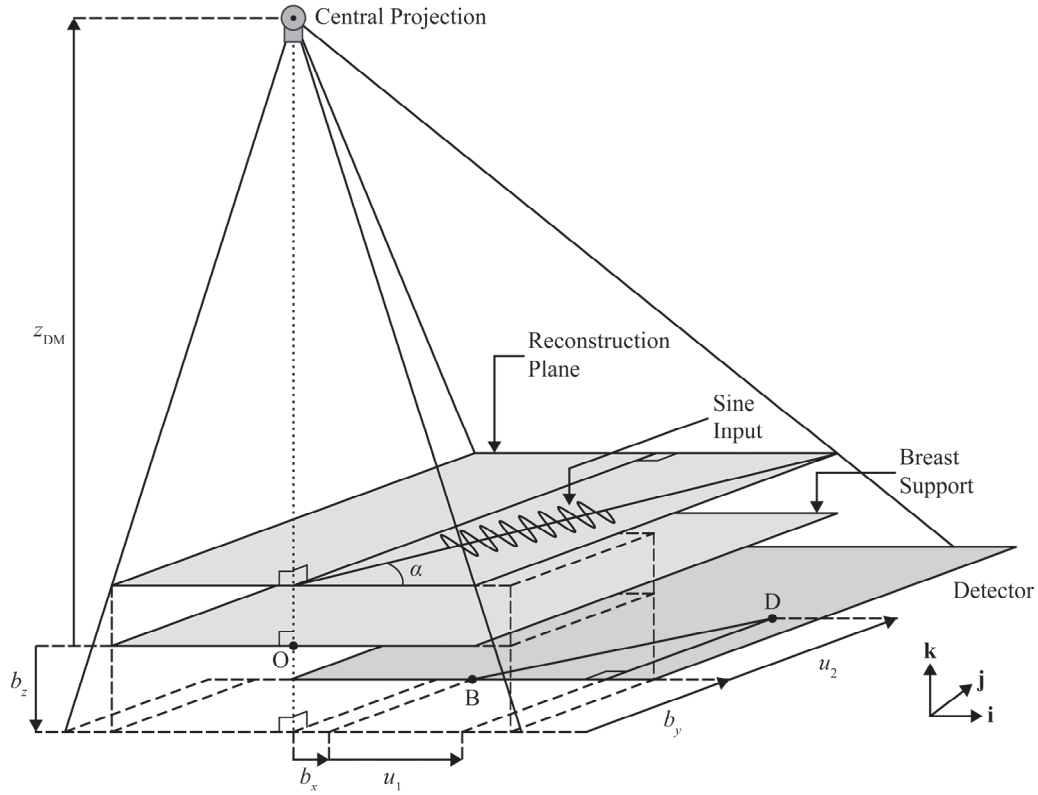
Figure 2. The detector translation relative to the origin O is illustrated in three dimensions. Also, the input frequency is oriented along the polar angle α in a plane parallel to the breast support.

The equation of the ray can thus be written using the parametric equations: $x = w\zeta_x + x_{FS}$, $y = w\zeta_y$, and $z = w\zeta_z + z_{FS}$. In these expressions, w is a free parameter ranging between zero and unity. As shown, the ray intercepts the input object between the depths $z = z_0 \pm \varepsilon/2$. The values of w corresponding to these two depths are $w^{\pm} = [z_0 \pm (1/2)\varepsilon - z_{FS}] / \zeta_z$. All values between w^+ and w^- correspond to ray positions within the object. The x-ray attenuation $\mathcal{A}\mu$ along the ray is thus

$$\mathcal{A}\mu = \int_{\mathcal{L}} \mu \cdot ds , \quad ds = \sqrt{(dx/dw)^2 + (dy/dw)^2 + (dz/dw)^2}\, dw = \sqrt{\zeta_x^2 + \zeta_y^2 + \zeta_z^2}\, dw , \tag{6}$$

where ds is differential arc length along the line $\mathcal{L}$ defined by the ray. Hence

$$\mathcal{A}\mu = \kappa \cdot \int_{w^+}^{w^-} \cos\left[2\pi f_0 \left(\zeta_x \cos\alpha + \zeta_y \sin\alpha \right) w + \lambda \right] dw \tag{7}$$

$$= \frac{\kappa \cdot \left(\sin\left[2\pi f_0 \left(\zeta_x \cos\alpha + \zeta_y \sin\alpha \right) w^- + \lambda \right] - \sin\left[2\pi f_0 \left(\zeta_x \cos\alpha + \zeta_y \sin\alpha \right) w^+ + \lambda \right] \right)}{2\pi f_0 \left(\zeta_x \cos\alpha + \zeta_y \sin\alpha \right)} , \tag{8}$$

where

$$\kappa = C_{\text{obj}} \cdot \sqrt{\zeta_x^2 + \zeta_y^2 + \zeta_z^2} , \quad \lambda = 2\pi f_0 \left[\left(x_{FS} - x_0 \right) \cos\alpha - y_0 \sin\alpha \right]. \tag{9}$$

By using a sum-to-product trigonometric identity and substituting the values for w^+ and w^-, it can be shown that

$$\mathcal{A}\mu = -\varepsilon \kappa \zeta_z^{-1} \cdot \cos\left[2\pi f_0 \zeta_z^{-1} \left(\zeta_x \cos\alpha + \zeta_y \sin\alpha \right) \left(z_0 - z_{FS} \right) + \lambda \right] \cdot \text{sinc}\left[\varepsilon f_0 \zeta_z^{-1} \left(\zeta_x \cos\alpha + \zeta_y \sin\alpha \right) \right], \tag{10}$$

where $\text{sinc}(u) \equiv \sin(\pi u)/(\pi u)$. This expression represents the signal recorded by the x-ray converter, assuming no sources of noise or blurring. To model a digital system, it is necessary to integrate Eq. (10) over the area of a detector element.

$$\mathcal{D}\mu(m_x, m_y) = \int_{a_y m_y}^{a_y(m_y+1)} \int_{a_x(m_x-1/2)}^{a_x(m_x+1/2)} \mathcal{A}\mu \frac{du_1}{a_x} \frac{du_2}{a_y} \tag{11}$$

$$= \lim_{J_{\mathrm{del},2} \to \infty} \frac{1}{J_{\mathrm{del},2}} \sum_{j_{\mathrm{del},2}=1}^{J_{\mathrm{del},2}} \left[\lim_{J_{\mathrm{del},1} \to \infty} \frac{1}{J_{\mathrm{del},1}} \sum_{j_{\mathrm{del},1}=1}^{J_{\mathrm{del},1}} \mathcal{A}\mu \Big|_{u_1 = a_x \left(\frac{j_{\mathrm{del},1}-1/2}{J_{\mathrm{del},1}} + m_x - \frac{1}{2} \right)} \right]_{u_2 = a_y \left(\frac{j_{\mathrm{del},2}-1/2}{J_{\mathrm{del},2}} + m_y \right)} \tag{12}$$

In Eq. (12), m_x and m_y are integer indices that determine the position of each detector element, and the area of each detector element is $a_x \times a_y$. A middle sum is used to evaluate the integral numerically.

2.3 Image Reconstruction

The reconstruction is now calculated using simple backprojection (SBP). While many software applications use filtering, an analysis of filtering is beyond the scope of this paper. Future work can explore how the filter can be optimized for super-resolution, as discussed in Section 4. To determine the backprojected signal at each point in space, a ray between the focal spot and the coordinate (x, y, z) is now considered. Using a computer algebra system (Maple 16, Maplesoft, Waterloo, Ontario), one can solve the parametric equations of the ray for the detector coordinates u_1 and u_2.

$$u_{1,\mathrm{SBP}} = \frac{x(b_z - z_{\mathrm{FS}}) - z(b_x - x_{\mathrm{FS}}) + b_x z_{\mathrm{FS}} - b_z x_{\mathrm{FS}}}{(z - z_{\mathrm{FS}})\cos\gamma - (x - x_{\mathrm{FS}})\sin\gamma} \tag{13}$$

$$u_{2,\mathrm{SBP}} = \frac{x b_y \sin\gamma + y\left[(b_z - z_{\mathrm{FS}})\cos\gamma - (b_x - x_{\mathrm{FS}})\sin\gamma\right] - z b_y \cos\gamma + b_y z_{\mathrm{FS}}\cos\gamma - b_y x_{\mathrm{FS}}\sin\gamma}{(z - z_{\mathrm{FS}})\cos\gamma - (x - x_{\mathrm{FS}})\sin\gamma} \tag{14}$$

The indices of the detector element corresponding to the detector coordinate described by Eqs. (13)-(14) are

$$m_{x,\mathrm{SBP}} = \left\lfloor (u_{1,\mathrm{SBP}} + a_x/2)/a_x \right\rfloor, \qquad m_{y,\mathrm{SBP}} = \left\lfloor u_{2,\mathrm{SBP}}/a_y \right\rfloor, \qquad \lfloor v_1 \rfloor \equiv \max\left\{ v_2 \in \mathbb{Z} : v_2 \le v_1 \right\}, \tag{15}$$

where $\lfloor\ \rfloor$ is the floor function. Using Eq. (15), the SBP reconstruction can be written

$$\mu_{\mathrm{SBP}} = (1/N) \cdot \sum_n \mathcal{D}\mu(m_{x,\mathrm{SBP}}, m_{y,\mathrm{SBP}}) . \tag{16}$$

A rotation matrix can be introduced to evaluate the reconstruction along the direction of the input frequency

$$\begin{pmatrix} x \\ y \\ z \end{pmatrix} = \begin{pmatrix} x_0 \\ y_0 \\ z_0 \end{pmatrix} + \begin{pmatrix} \cos\alpha & -\sin\alpha & 0 \\ \sin\alpha & \cos\alpha & 0 \\ 0 & 0 & 1 \end{pmatrix} \begin{pmatrix} x'' \\ y'' \\ z'' \end{pmatrix}, \tag{17}$$

where x'' denotes position along the polar angle α.

2.4 Fourier Transform of the Reconstruction

To determine whether the sine plate is resolved in the reconstruction, the one-dimensional (1D) Fourier transform is now calculated along the direction of the polar angle α. The frequency variable of this transform is denoted f_x'' [Eq. (18)]. In a perfect reconstruction, the Fourier transform would have peaks at the frequencies $f_x'' = \pm f_0$ and would be zero at all other frequencies. Eq. (18) shows how this integral can be calculated using a middle sum.

$$\mathcal{F}_1 \mu_{\mathrm{SBP}} \approx \int_{x''_{\min}}^{x''_{\max}} \mu_{\mathrm{SBP}} e^{-2\pi i f_x'' x''} dx'' = \lim_{J_{\mathrm{FT}} \to \infty} \left(\frac{x''_{\max} - x''_{\min}}{J_{\mathrm{FT}}} \right) \sum_{j_{\mathrm{FT}}=1}^{J_{\mathrm{FT}}} \mu_{\mathrm{SBP}} e^{-2\pi i f_x'' x''} \Big|_{x'' = x''_{\min} + (x''_{\max} - x''_{\min})\left(\frac{j_{\mathrm{FT}}-1/2}{J_{\mathrm{FT}}} \right)} \tag{18}$$

While the integration limits of a Fourier transform typically range from $-\infty$ to $+\infty$, it is useful to introduce a narrower range in order to measure the local properties of the Fourier transform. This setup allows for measurement of anisotropies that vary with position. For the purpose of this work, it will be assumed that $x''_{\min} = -5.0\ \mathrm{mm}$ and that $x''_{\max} = 5.0\ \mathrm{mm}$, so that 50 cycles are considered for an input frequency of 5.0 mm^{-1}.
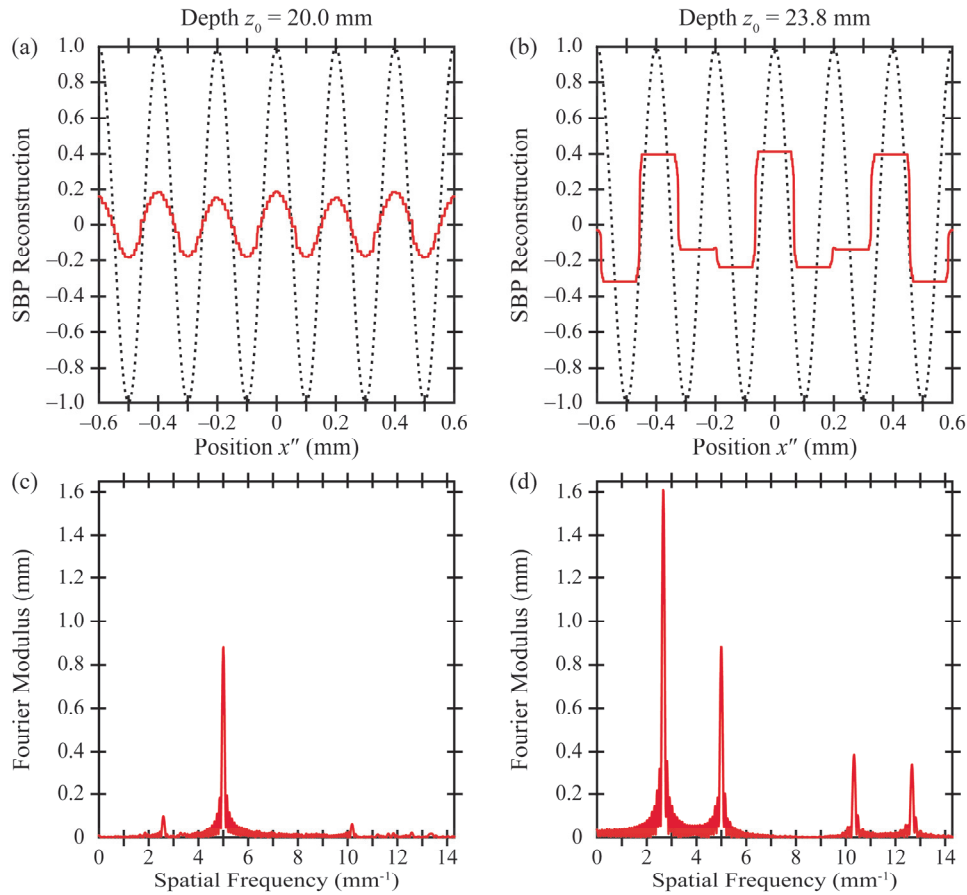
Figure 3. (a) A high-frequency input (5.00 mm^{-1}) is properly resolved at the depth $z_0 = 20.0$ mm. (b) By contrast, the input is not resolved at the depth $z_0 = 23.8$ mm. This result demonstrates the depth-dependency of super-resolution. (c) The Fourier transform is used to illustrate super-resolution at the depth $z_0 = 20.0$ mm. (d) At the depth $z_0 = 23.8$ mm, the frequency corresponding to the major peak of the Fourier Transform (2.66 mm^{-1}) is lower than the input frequency. This result provides evidence of aliasing at this depth.

3. RESULTS

3.1 Modeling the Conventional Acquisition Geometry

To illustrate the model of super-resolution in the conventional acquisition geometry, Figure 3 shows a simulation of the Selenia Dimensions system (Hologic Inc., Bedford, MA). The acquisition parameters for this system can be summarized by the expressions: $N = 15$, $\Delta\psi = 1.07°$, $z_{DM} = 675.0$ mm, $z_{COR} = -25.0$ mm, $b_x = b_y = 0$, $b_z = -25.0$ mm, and $a_x = a_y = 0.140$ mm. To investigate super-resolution, it is necessary to specify the frequency of the sine plate to be higher than the alias frequency of the detector (3.57 mm^{-1}). In this paper, an input frequency (f_0) of 5.00 mm^{-1} is chosen. Additional parameters for the sine plate are as follows: $\varepsilon = 0.50$ mm, $C_{obj} = 2.0$ mm^{-1}, $\alpha = 0°$, $x_0 = 0$, and $y_0 = 60.0$ mm.

Two depths (z_0) are now considered to illustrate how the feasibility of super-resolution is dependent on position in the reconstruction. The reconstructions at each depth are evaluated as a function of x'' assuming that $y'' = 0$ and $z'' = 0$ using MATLAB® (Natick, MA). Figure 3(a) shows that all the peaks and troughs of the sine plate are resolved at the depth $z_0 = 20.0$ mm, providing evidence of super-resolution. By contrast, Figure 3(b) indicates that the reconstruction appears step-like at the depth $z_0 = 23.8$ mm, with the width of each step matching the detector element size (0.140 mm). Thus, the depth of 23.8 mm is an example of a position at which super-resolution cannot be achieved.

Figures 3(c)-(d) show the Fourier transforms of the two simulations described above. At the depth $z_0 = 20.0$ mm, the Fourier transform has a major peak at the input frequency (5.00 mm^{-1}). This result is expected, since super-resolution is clearly seen in Figure 3(a). By contrast, at the depth $z_0 = 23.8$ mm, the major peak of the Fourier transform corresponds to the frequency 2.66 mm^{-1}.
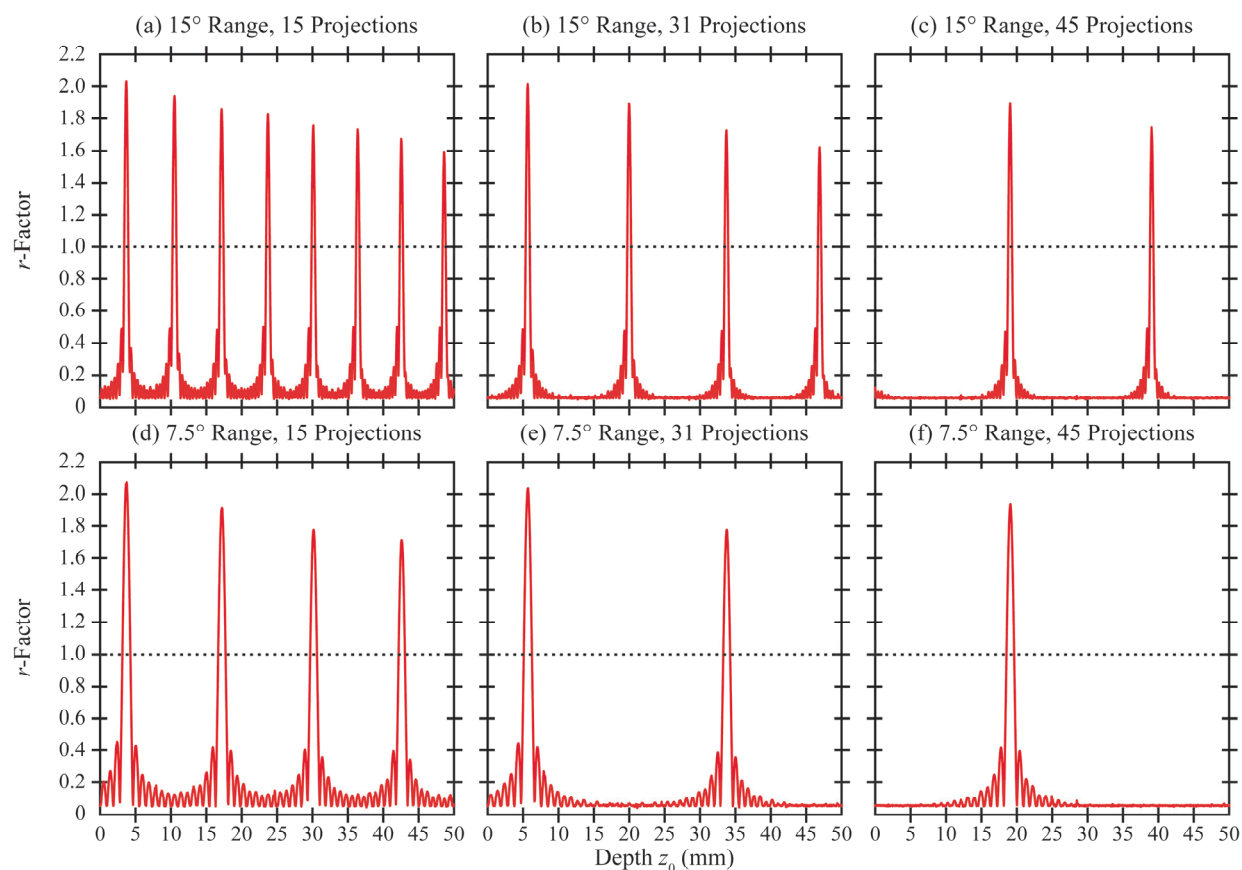
Figure 4. A metric that can be derived from the Fourier transforms of Figure 3 is the r-factor. This metric is the ratio of the amplitude of the largest peak less than 5.00 mm^{-1} to the amplitude at 5.00 mm^{-1}. The r-factor is used to identify the depths (z_0) at which super-resolution cannot be achieved; specifically, the depths corresponding to the sharp peaks. As shown, there are two ways to increase the spacing between peaks and hence to optimize super-resolution: (1) increase the number of projections (N), or (2) reduce the angular range of the scan.

Our previous work[4,6] introduced a Fourier ratio metric (r) to quantify the aliasing that is illustrated by Figure 3(d). The r-factor is defined as the ratio of the amplitude of the largest peak less than 5.00 mm^{-1} to the amplitude of the peak at 5.00 mm^{-1}. In general, super-resolution is achieved if $r < 1$, but aliasing is observed if $r \geq 1$. Figure 3(d) shows that $r = 1.83$ at the 23.8 mm depth, indicating that super-resolution is not achieved.

To identify all the depths lacking super-resolution, the r-factor is plotted as a function of z_0 in Figure 4. In the Selenia Dimensions system [Figure 4(a)], there are eight depths between 0 and 50.0 mm above the breast support at which super-resolution cannot be achieved. Figure 4 illustrates that one way to minimize the number of peaks in this plot is to increase the number of projections (N). There are four peaks if 31 projections are used [Figure 4(b)], and there are two peaks if 45 projections are used [Figure 4(c)]. Increasing the number of projections in this manner is equivalent to reducing the angular spacing between projections ($\Delta\psi$), since the angular range of the scan (15°) is held constant. Hence, this approach provides a strategy for reducing the number of anisotropies in the conventional acquisition geometry.

In Figure 4(d)-(f), a system with a smaller angular range (7.5°) is modeled. Similar to subplots (a)-(c), subplots (d)-(f) show that the spacing between peaks is increased as the number of projections (N) is increased. Additionally, it is demonstrated that there are fewer peaks in subplots (d)-(f) than in subplots (a)-(c). For example, if 15 projections are used, there are eight peaks in a system with a 15° angular range [Figure 4(a)], yet there are four peaks in a system with a 7.5° angular range [Figure 4(d)]. This result provides further evidence that the use of a smaller angular spacing between projections yields fewer anisotropies in the conventional design. In the example with 15 projections, the angular spacing between projections is reduced from 1.07° in Figure 4(a) to 0.536° in Figure 4(d).
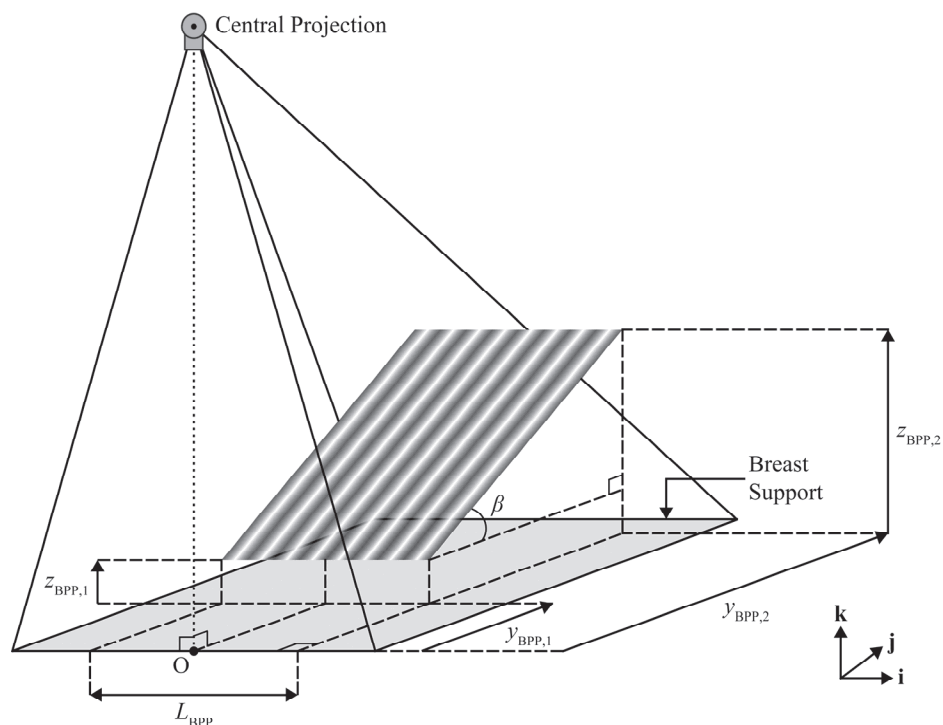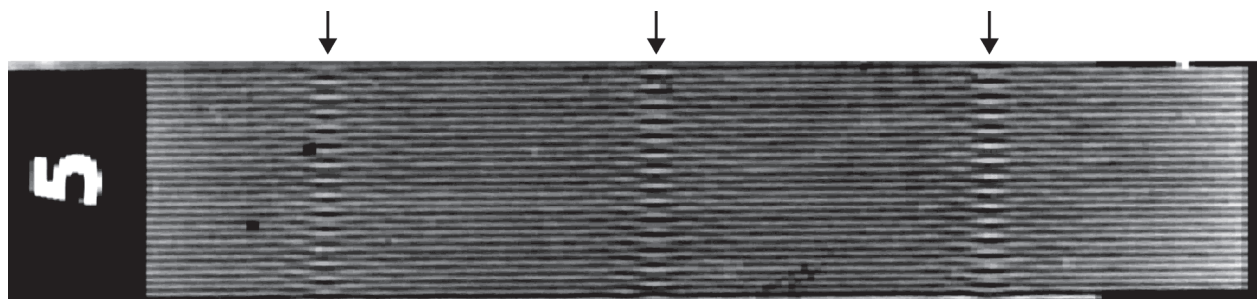
Figure 5. The depth-dependency of super-resolution was validated experimentally using a bar pattern phantom. To analyze a range of depths (z) in one image, the plane of the bar pattern phantom was oriented at an angle ($\beta = 46.5°$) relative to the breast support. Also, the test frequency was oriented along the polar angle (α) of $0°$; this polar angle matches the simulations of Section 3.1.

3.2 Experimental Validation

To validate the anisotropies experimentally, a bar pattern phantom was imaged using the Selenia Dimensions system. One way to observe the anisotropies is to orient the bar pattern phantom in a plane parallel to the breast support, and then re-position the phantom at multiple depths (z). While this approach was used in the theoretical model of Section 3.1, it would be inefficient experimentally, as it would require numerous x-ray acquisitions. A more efficient approach is to orient the bar pattern phantom at an oblique angle using a goniometry stand, as shown in Figure 5. This approach allows for visualization of a continuous range of depths (z) in a single x-ray acquisition. Although the plane of the bar pattern phantom is oblique relative to the breast support, the frequency itself is parallel to the breast support and is directed along the polar angle (α) of $0°$, as was considered in Section 3.1.

In these experiments, the middle bar of the frequency 5.0 mm^{-1} was roughly aligned with the mid-plane that divides the breast support into two equal halves, as shown in Figure 5. The technique factors for the scan were 30 kVp and 25 mAs with a W/Al target-filter combination. In addition, the following values for the parameters shown in Figure 5 were used: $\beta = 46.5°$, $L_{BPP} = 6.0$ mm, $y_{BPP,1} = 56.8$ mm, $y_{BPP,2} = 77.0$ mm, $z_{BPP,1} = 10.7$ mm, and $z_{BPP,2} = 31.8$ mm.

Figure 6. An oblique reconstruction in the plane of the bar pattern phantom shows the depth-dependency of super-resolution.

Figure 6 shows a reconstruction of the bar pattern phantom using Piccolo™ (Real Time Tomography, LLC, Villanova, PA). This software[7] has a feature which allows the user to align the plane of reconstruction with the oblique plane of the phantom. Aliasing artifacts are observed at the arrows. Super-resolution can be seen in the other regions of the image. In the z direction, there are 6.34 and 6.49 mm spacing between the centroids of adjacent aliasing artifacts. The spacing is predicted correctly by the theoretical model to within absolute errors of 0.07 and 0.06 mm, respectively.

3.3 Modeling Detector Translation During the Scan

The results of Sections 3.1 and 3.2 suggest that super-resolution is not achievable at all positions in the conventional design. In previous work, a new form of detector motion was proposed to optimize super-resolution.[6] That work considered detector translation along the y direction (*i.e.*, the PA direction) to eliminate the anisotropies along the polar angle $\alpha = 90°$. This paper proposes a more general form of detector motion, in which the detector is also translated along the z direction. This motion is being considered to eliminate the z-dependency of super-resolution, which was observed in Sections 3.1 and 3.2 along the polar angle $\alpha = 0°$. It should be pointed out that x translation is not modeled ($b_x = 0$).

$$b_y = \begin{cases} b_{y1} + T_y^{-1}(b_{y2} - b_{y1})T, & 0 \leq T < T_y \\ b_{y2} + (T_t - T_y)^{-1}(b_{y3} - b_{y2})(T - T_y), & T_y \leq T \leq T_t \end{cases}, \quad b_z = \begin{cases} b_{z1} + T_z^{-1}(b_{z2} - b_{z1})T, & 0 \leq T < T_z \\ b_{z2} + (T_t - T_z)^{-1}(b_{z3} - b_{z2})(T - T_z), & T_z \leq T \leq T_t \end{cases} \quad (19)$$

Recall that b_x, b_y, and b_z are the coordinates of point B of the detector (Figures 1-2). Unlike previous work which considered monotonic detector translation, this paper models a more general form of motion with up to one turn. As such, the y-coordinate of point B varies between b_{y1} at time $T = 0$, b_{y2} at time $T = T_y$ (the time point of the turn), and b_{y3} at time $T = T_t$ (the end time). Similar notation is used for the z-coordinate. The detector position for the nth projection can be determined from the substitution: $T = T_t \cdot (n - 1) / (N - 1)$. For the purpose of this paper, it is assumed that both the focal spot and the detector are stationary during each projection, and hence there is no motion blurring.

To illustrate the new form of detector motion, the z-coordinate of point B is plotted as a function of the projection number (n) in Figure 7(a). Unlike Section 3.1, it is assumed that there is no detector rotation. Also, it is assumed that there is a 10.0 mm gap between the breast support and the detector at the start of the scan ($b_{z1} = -10.0$ mm). Figure 7(a) shows how the detector is translated along the $-z$ direction during the first half of the scan, and then translated along the $+z$ direction during the second half of the scan. The position of the turn (*i.e.*, the cusp) is controlled by the parameter b_{z2}, as shown by four sample values. This plot has been prepared with parameters that ensure symmetry about the mid-time.

The r-factor is now evaluated for the four detector trajectories of Figure 7(a). One way to compare the trajectories is to calculate the r-factor at every point in the image. However, it would not be practical to calculate the r-factor at this many points due to the long computation time. A simulation of 1,000 randomly chosen points is now considered instead. For this calculation, a volume-of-interest (VOI) is defined with dimensions $200.0 \times 100.0 \times 50.0$ mm and a spacing of 0.050 mm between points in each direction. The VOI is centered on the point (0, 50.0, 25.0) in mm. Figure 7(b) illustrates how this simulation can be used to create a histogram of r-factor values for the special case of a stationary detector. The polar angle (α) of 0° is considered, similar to Section 3.1. The histogram shows that 100 points (10.0% of the image volume) possess an r-factor of unity or greater. These points are characterized by the presence of aliasing.

To compare the four detector trajectories of Figure 7(a), cumulative histograms of the r-factor are now calculated. First, a simulation with no translation along the y direction is considered ($b_{y1} = b_{y2} = b_{y3} = 0$), as shown in Figure 7(c). If a conventional design with no detector translation along the z direction is used ($b_{z2} = -10.0$ mm), it can be seen that the r-factor exceeds unity at some positions in the image. The use of detector translation along the z direction ensures that the r-factor does not exceed unity at any position in the image, yielding an improvement in image quality. These results hold for both polar angles ($\alpha = 0°$ and 90°). Figure 7(c) also illustrates that the position of the plateau corresponding to the maximum r-factor is shifted to the left by increasing the net motion along the z direction. Hence, the use of a larger range of z motion is beneficial, since super-resolution with high quality is achieved if the r-factor is as small as possible.

Similar simulations are shown for a detector with translation along the y direction [Figure 7(d)]. The net motion that is modeled along the y direction is 0.30 mm ($b_{y1} = 0$, $b_{y2} = 0.30$ mm, $b_{y3} = 0$). For frequency measurements along the 90° polar angle, super-resolution is achieved at all positions in the image, even without the use of translation along the z direction. This result is expected from our previous work, which proposed the idea of translation along the y direction.[6] However, for frequency measurements along the 0° polar angle, detector translation along the y direction is not sufficient for achieving super-resolution at all positions in the image. For this reason, detector translation along the z direction is an important design modification that ensures super-resolution along both polar angles.
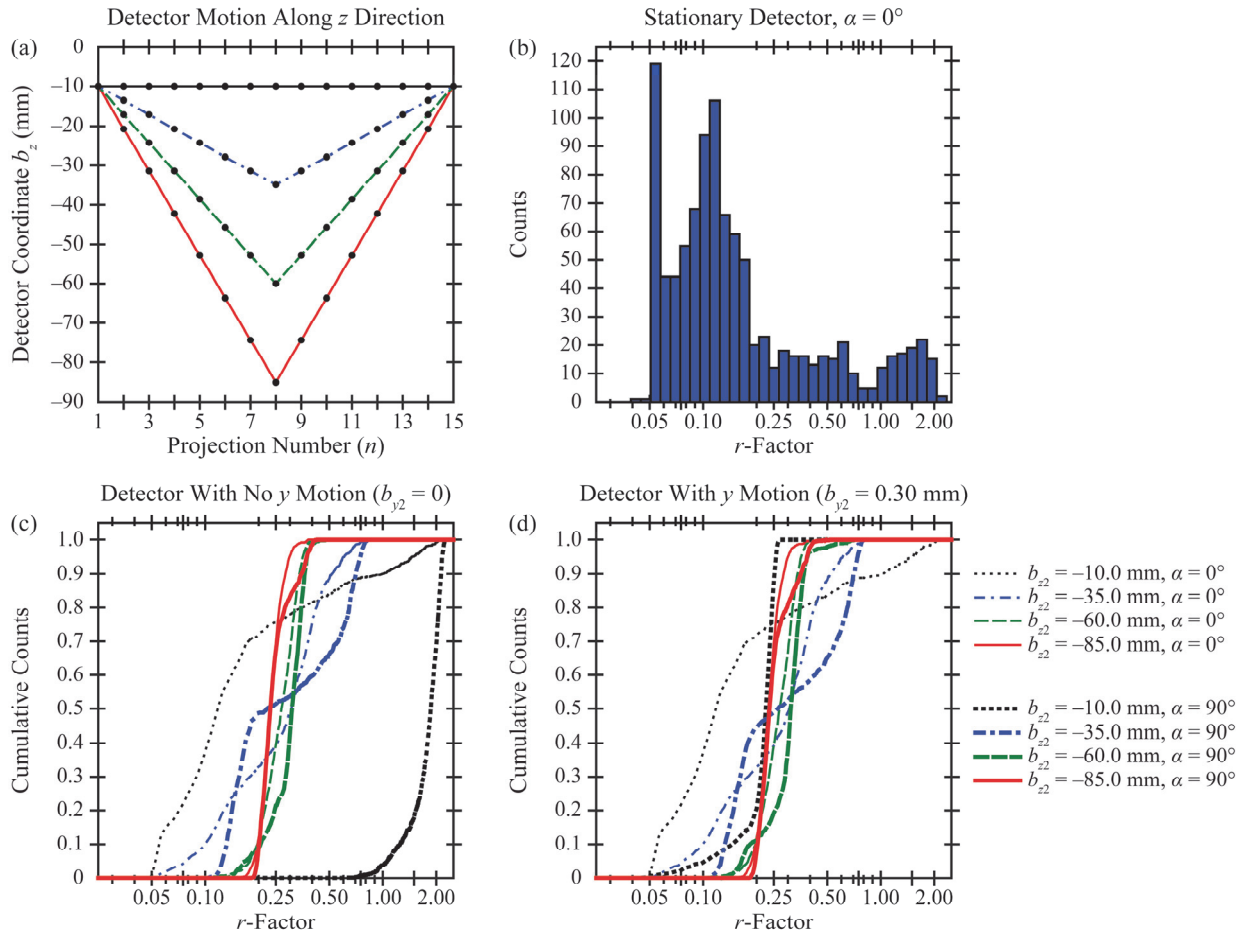
Figure 7. (a) Detector trajectories along the z direction are shown using four sample values of b_{z2}. (b) Assuming that the detector is stationary ($b_{z1} = b_{z2} = b_{z3} = -10.0$ mm) and that frequency is measured along the polar angle (α) of 0°, a histogram of r-factor values is created from 1,000 randomly chosen points in the image volume. (c) Cumulative histograms are calculated for a detector with no motion along the y direction. (d) Cumulative histograms are similarly calculated for a detector with motion along the y direction.

To compare the detector trajectories further, it is useful to calculate the 95th percentile of each cumulative histogram. Demonstrating that this percentile is well below unity ensures that at least 95% of the points in the image exhibit super-resolution with high quality. Figure 8 demonstrates how a 95% confidence interval (CI_{95}) can be determined for the 95th percentile using 400 bootstrapped simulations of 1,000 randomly chosen points. In the special case of a stationary detector and a polar angle (α) of 0°, Figure 8(a) illustrates the histogram of 400 values obtained for the 95th percentile. Figure 8(b) shows that the quantile-quantile plot for this histogram lies roughly along a 45° line, suggesting normality.

By analyzing the middle 95% of data points in histograms comparable to Figure 8(a), the CI_{95} was calculated for multiple detector trajectories [Figure 8(c)-(d)]. At first glance, it would appear that the best trajectory is the one with y motion and no z motion ($b_{z2} = -10.0$ mm); this result is seen in Figure 8(d) along the 90° polar angle. However, this trajectory does not optimize super-resolution along the 0° polar angle, since the CI_{95} exceeds unity. Thus, it should be emphasized that z motion is necessary for ensuring that high-quality super-resolution is achieved along both polar angles.

4. DISCUSSION AND CONCLUSION

Our previous work demonstrated that super-resolution is a mechanism for improving calcification visibility in DBT, but that super-resolution cannot be achieved at all positions in the image volume. Specifically, super-resolution cannot be achieved at all depths (z) above the breast support.[4] While our previous work on the depth-dependency of super-resolution was purely theoretical, this paper provides experimental evidence of the anisotropy. Also, unlike previous
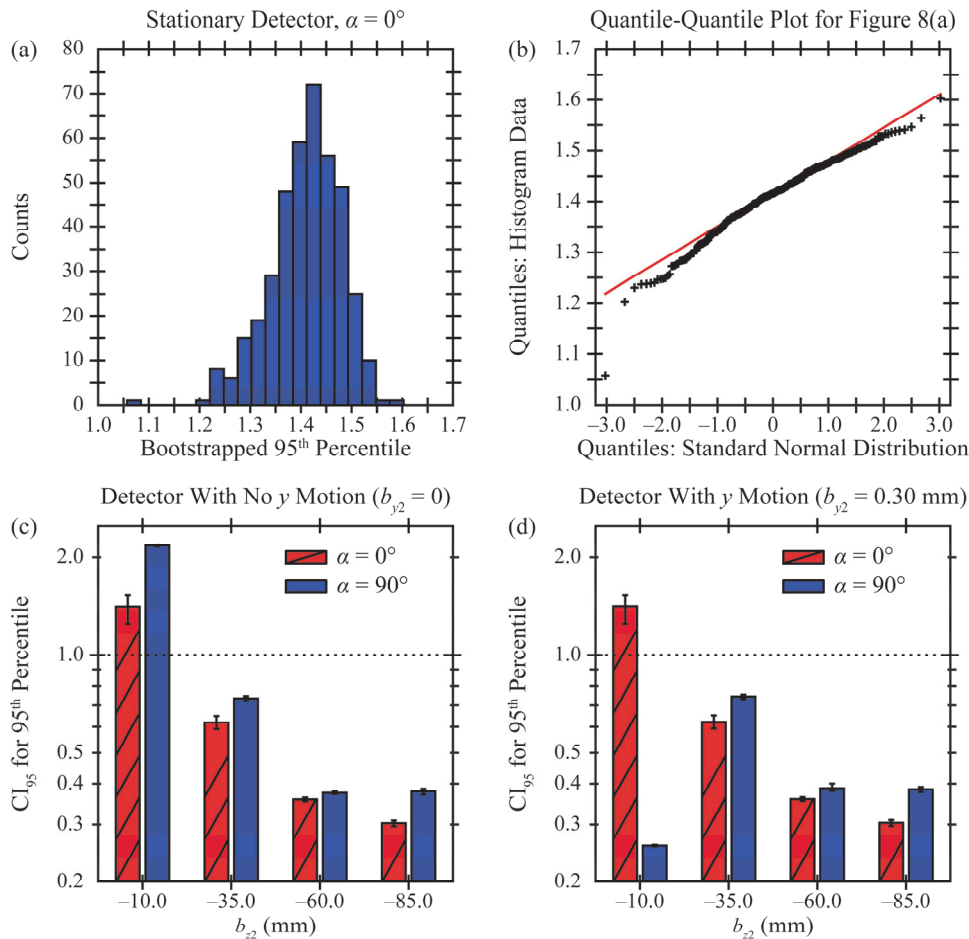
Figure 8. (a) The *r*-factor was calculated using 400 bootstrapped simulations of 1,000 randomly chosen points in the image volume. The 95th percentile of the *r*-factor was then determined in each of the 400 bootstrapped simulations. This approach yields a histogram of 400 values for the 95th percentile. The 95th percentile provides a bound on the quality of super-resolution that is observed in 95% of the points in the image volume. (b) The quantile-quantile plot for the 400 bootstrapped values of the 95th percentile lies roughly along the 45º line, suggesting normality. (c) The 95th percentile was calculated for all cumulative histograms shown in Figure 7(c). A 95% confidence interval was determined from bootstrapping. (d) Similar results are shown for the 95th percentile of the cumulative histograms of Figure 7(d).

work, design strategies that minimize the number of anisotropies are identified. Using a theoretical model of a high-frequency test object, it is demonstrated that reducing the angular spacing between projections allows for broader spacing between anisotropies and hence an improvement in image quality.

Although the number of anisotropies can be minimized by reducing the spacing between projections, it may not be possible to eliminate the anisotropies entirely using this approach. In particular, it was determined that anisotropies are still present even if the number of projections is increased from 15 to 45 (Figure 4). For this reason, another approach needs to be considered in order to optimize super-resolution at all positions in the image. In Section 3.3, a new form of detector motion along the *z* direction was proposed, and this motion was found to yield super-resolution everywhere.

To demonstrate the benefits of the new detector trajectory, 1,000 points in the image were chosen at random and a cumulative histogram of the *r*-factor was calculated. The 95th percentile was used to determine an upper bound on the *r*-factor that is achieved by 95% of the points in the image. In addition, bootstrapped simulations were used to create 95% confidence intervals. It was found that, if the range of *z* motion is increased, the 95th percentile decreases in magnitude. This result indicates an improvement in the quality of super-resolution. The confidence intervals in Figure 8 are sufficiently narrow in order to ensure that enough points were chosen at random to demonstrate the benefit of a larger range of *z* motion.

If this detector trajectory is implemented clinically, it may be necessary to increase the thickness of the detector housing in order to accommodate the range of z motion that is proposed. The thickness of the detector housing at the chest wall side of a clinical system is roughly 70 mm. In this paper, the trajectory with a net z motion of 75.0 mm ($b_{z2} = -85.0$ mm) clearly does not fit within the thickness of a typical detector housing. One trade-off of increasing the thickness of the detector housing is that positioning the patient for the DBT scan may become more cumbersome. While the theoretical model suggests that increasing the thickness of the detector housing is beneficial, future work is necessary to determine the largest thickness that is practical for patients.

While this paper assumes a point-like focal spot, future work should model the blurring due to the finite size of the focal spot. One drawback of the detector trajectory being proposed is that the magnification increases as the range of z motion is increased. Previous work has shown that the modulation transfer function of the focal spot is degraded with increasing magnification.[8] In future work, it is important to determine whether modulation is preserved in detector trajectories with a large range of z motion.

In this paper, 1,000 points were chosen at random from a VOI having the shape of a rectangular prism. Only one VOI with dimensions $200.0 \times 100.0 \times 50.0$ mm was considered. One limitation of this approach is that there was no analysis of how the size and positioning of the VOI can impact the calculation of the r-factor. An additional limitation is that the VOI is not anatomical in shape. Future work can determine whether the cumulative histogram of the r-factor is dependent on the size, shape, and positioning of the VOI.

An additional limitation of this paper is that the effect of the reconstruction filter was not modeled. It is expected that the filter will have an impact on the r-factor, since the filter controls the relative weight given to each frequency in Fourier space. Future work is merited to determine whether the filter can be optimized to reduce the magnitude of the r-factor relative to the values presented in this paper.

5. ACKNOWLEDGEMENT

6. REFERENCES

1. Poplack SP, Tosteson TD, Kogel CA, Nagy HM. Digital Breast Tomosynthesis: Initial Experience in 98 Women with Abnormal Digital Screening Mammography. *American Journal of Roentgenology.* 2007;189:616-623.
2. Rafferty EA, Park JM, Philpotts LE, et al. Assessing Radiologist Performance Using Combined Digital Mammography and Breast Tomosynthesis Compared with Digital Mammography Alone: Results of a Multicenter, Multireader Trial. *Radiology.* 2013;266(1):104-113.
3. Friedewald SM, Rafferty EA, Rose SL, et al. Breast Cancer Screening Using Tomosynthesis in Combination With Digital Mammography. *Journal of the American Medical Association.* 2014;311(24):2499-2507.
4. Acciavatti RJ, Maidment ADA. Observation of super-resolution in digital breast tomosynthesis. *Medical Physics.* 2012;39(12):7518-7539.
5. Hsieh J. Chapter 7: Image Artifacts: Appearances, Causes, and Corrections. *Computed Tomography: Principles, Design, Artifacts, and Recent Advances*. Bellingham, WA: SPIE Press; 2003:167-240.
6. Acciavatti RJ, Maidment ADA. Proposing an Acquisition Geometry That Optimizes Super-Resolution in Digital Breast Tomosynthesis. *Lecture Notes in Computer Science.* 2012;7361:386-393.
7. Kuo J, Ringer PA, Fallows SG, Bakic PR, Maidment ADA, Ng S. Dynamic Reconstruction and Rendering of 3D Tomosynthesis Images. Paper presented at: SPIE Medical Imaging2011; Lake Buena Vista, FL.
8. Johns HE, Cunningham JR. Chapter 16: Diagnostic Radiology. *The Physics of Radiology*. 4th ed. Springfield, IL: Charles C Thomas; 1983:557-669.